Ultrafine Si nanowires/Sn$_3$O$_4$ nanosheets 3D hierarchical heterostructured array as a photoanode with high-efficient photoelectrocatalytic performance

Ruiqi Yang[a], Yanchen Ji[a], Qiang Li[b], Zhenhuan Zhao[b], Ruitong Zhang[a], Linlin Liang[a], Fan Liu[a], Yuke Chen[a], Shuwei Han[a], Xin Yu[a,*], Hong Liu[a,c,*]

[a] Institute for Advanced Interdisciplinary Research (iAIR), University of Jinan, Jinan 250022, PR China
[b] School of Advanced Materials and Nanotechnology, Xidian University, Xi'an, 710071, PR China
[c] State Key Laboratory of Crystal Material, Shandong University, Jinan 250100, PR China

ABSTRACT

Constructing a high performance three-dimensional (3D) semiconductor photoelectrode for photoelectrocatalytic hydrogen (H$_2$) production by water splitting is a promising method to resolve the current energy and environmental issues. Here, a ultrafine Si nanowires/Sn$_3$O$_4$ nanosheet (SiNWs/Sn$_3$O$_4$) 3D hierarchical heterostructured photoanode was synthesized *via* a facile approach with a metal-assisted chemical etching step following an *in situ* hydrothermal synthesis process. The ultrafine SiNWs/Sn$_3$O$_4$ 3D hierarchical heterostructured photoanode exhibits significantly enhanced photoelectrochemical activity, and its photocurrent density is 8 times higher than that of single phase structures of SiNWs. This increase of catalytic activity may be attributed to the enhancement of the full-spectrum light absorption, decrease of the photocarrier recombination rate and a low transmission resistance at the catalyst/electrolyte interface. This work provides a novel design for preparing highly efficient Si based 3D heterostructured catalysts for the production of clean energy.

1. Introduction

Hydrogen (H$_2$) is a green renewable fuel with high energy density and has been known as the potential alternative to fossil fuels [1–3]. Photocatalytic H$_2$ production by water splitting with semiconductor catalyst has attracted extensive research interest as it may be a promising approach to resolve the energy shortage and environmental pollution problems [4–7]. Fujishima and Honda reported for the first time the potential of TiO$_2$ semiconductor photocatalysts for the photocatalytic water splitting to produce hydrogen and oxygen [8]. Based on their work, the majority of researchers started to pay attention to the development and application of semiconductor photocatalysts in energy and environment fields [9–11]. Disappointingly, although some kinds of semiconductors possess high light-electric conversion ability, the recombination of photo-induced carrier causes low photocatalysis performance [12]. To overcome the photocarrier recombination, photoelectrocatalysis technique and the photoelectrode designed for photoelectocatalysis have suggested and developed. However, up to now, most high performance photoelectrocatalysts are granular composites, which need to be mixed with binder and coated on conducting substrates to form photoelectrodes [13]. There are many defects in the preparation of granular composite electrodes: (1) Semiconductor

organic binder coating has poor conductivity, and the blocking effect on light absorption and carrier transport severely inhibits photoelectrocatalytic activity; (2) The flat surface of the granular composite electrodes have a small specific surface area; (3) The catalyst may be detached during the reaction due to the weak binder; (4) The preparation process is complicated and need to carefully operating. Therefore, the development of a three-dimensional (3D) sheet-like hierarchical heterostructure photoanode catalyst with excellent activity for photoelectrochemical (PEC) water splitting is an effective means to address the problems of the granular photoelectrode materials. The 3D sheet-like heterostructure electrode does not require the organic binder as a connecting agent between catalyst and conductive substrate, and thus has strong firmness, the excellent heterogeneous interface also promotes rapid transport of carriers. The 3D structure has a large specific surface area and provides more active sites for the redox reaction. Thus, the 3D sheet-like hierarchical heterostructure photoelectrode perfectly solves the defects of the granular composite electrodes.

Silicon (Si), as the earth's second most abundant element, is considered to be a promising candidate material for optoelectronic applications [14–16]. Si has a narrow indirect band gap of 1.12 eV, so it has excellent light absorption properties and can absorb solar energy from ultraviolet (UV) to near-infrared (NIR) light [17]. Although Si has an

appropriate band gap width and band edge location, the use of planar Si as a photoelectrode still poses great challenges due to slow kinetics and low active surface area [18]. In particular, one-dimensional Si nanostructures -Si nanowires (SiNWs) or Si microwires (SiMWs), have broad application prospects in the field of photoelectrocatalytic applications [19–22]. This is due to the fact that it not only has a large specific surface area compared to the bulk materials and zero-dimensional nanostructures, but more importantly, it can shorten the charge transport distance and reduce the recombination rate of photogenerated electron/hole pair [23]. There are different ways for preparing SiNWs, such as chemical vapor deposition [24], molecular beam epitaxy [25], metal-assisted chemical etching (MACE) method [26]. A published work proved that SiNWs still have a lower photoelectric conversion efficiency due to poor intrinsic kinetics at the SiNWs–electrolyte interface toward H_2 evolution reaction (HER) [5]. Previous studies have demonstrated that catalytic performance can be significantly improved by depositing noble metal co-catalyst on the SiNWs surface [27,28], whereas this cannot be widely application because of its high cost and scarcity. Therefore, combining with a photocatalytic semiconductor with appropriate bandgap would help to reduce the interface resistance and improve the catalytic reaction activity. Generally, metal or transition metal oxides have great applications in the photoelectrocatalytic field [29]. Tin oxide has the advantages of earth abundant, non-toxic, environmentally friendly [30–32], and Sn_3O_4 is a layer-structured oxide composed of Sn^{2+} and Sn^{4+} mixed valences [33]. Previous reports have shown that Sn_3O_4 can catalyze water splitting in visible light to produce H_2 [34]. Unfortunately, photocatalytic activity of Sn_3O_4 is not ideal due to the high carrier recombination rate during the reaction. Therefore, most of the previous studies required the deposition of noble metal as a co-catalyst to increase the catalytic activity of Sn_3O_4 under visible light [35], which brought greater consumption. In order to reduce costs and obtain excellent catalytic activity, it is reasonable to believe that the effective assembling of Sn_3O_4 nanosheet and SiNWs will solve the above problems and achieve the desired goal.

Herein we first reported the fabrication of SiNWs/Sn_3O_4 hierarchical heterostructured array photoanode by a metal-assisted chemical etching method following a facile hydrothermal step. The 3D structure has a large specific surface area, providing more light absorption area and active site of redox reaction; the heterogeneous interface between SiNWs and Sn_3O_4 promotes photocarrier separation and rapid transport; the unique structure makes the carrier transport path smaller, further suppressing the carrier recombination. The resulting SiNWs/Sn_3O_4 photoanode catalyst exhibits enhanced PEC water splitting activity, with short-circuit photocurrent density is about 8 times higher than that of single-phase structures of SiNWs photoanode. This work provides a new approach and an appropriate method for further research on the application of Si-based materials in photoelectrocatalysis.

2. Results and discussion

Fig. 1a exhibits the schematic of the synthetic process of the SiNWs/Sn_3O_4 hierarchical heterostructure photoanode, which is a facile process that include the MACE and hydrothermal methods. First, vertically aligned SiNWs array was synthesized by treating Si wafer in a mixture of HF and H_2O_2, as report previously [26]. Then, the Sn_3O_4 nanosheets densely grew in-situ on the SiNWs array by the hydrothermal step. The morphology of the as-prepared photoanodes were characterized using scanning electron microscope (SEM) and transmission electron microscopy (TEM) measurements. From the SEM images of the plane and cross section views of SiNWs (Fig. 1b and c), it can be concluded that the SiNWs are very dense and uniform vertically aligned on the Si substrate. The length is around 5 μm, and the diameter is around 100 nm. As shown in Fig. 1e, the TEM images further confirmed that. For separately synthesized Sn_3O_4, it shows a spherical microstructure aggregates assembled from a large number of nanosheets (Fig. S1a),

which average diameter is about 200 nm (Fig. S1b). The chemical analysis of Sn_3O_4 was analyzed by an energy-dispersion spectroscopy (EDS). The EDS spectrum is shown in Fig. S2 and S3. The molar ratio of Sn/O was calculated ~ 3:4 as from the peak intensities. After the in-situ growth of Sn_3O_4, the SiNWs was completely covered with small Sn_3O_4 nanosheets, forming a 3D SiNWs/Sn_3O_4 hierarchical heterostructure. The integrity of the nanowire array structure is well retained after the deposition of Sn_3O_4, and the Sn_3O_4 still retains spherical aggregates assembled from nanosheets. The HRTEM image (Fig. 1g) shows that Sn_3O_4 nanosheets have a clear crystalline lattice image (d_{111} = 0.329 nm and d_{101} = 0.366 nm) indicating its high crystallinity.

The powder X-ray diffraction (XRD) pattern of Sn_3O_4 nanosheets and SiNWs/Sn_3O_4 hierarchical heterostructure are shown in Fig. 2a. For Sn_3O_4 nanosheets, the peak positions are match well with standard Sn_3O_4 (JCPDS card, no. 16-0737) [36]. When Sn_3O_4 nanosheets are assembled on SiNWs to form SiNWs/Sn_3O_4 hierarchical heterostructure, the strong peak at 68.9° is attributed to the monocrystalline Si (PDF 27–1402) [37], and the characteristic peaks at 31.7°, 32.3°, 33.1°, 55.8°, 63.5°, 65.5° and 67.2° corresponding to the (−210), (121), (210), (2–41), (312), (033) and (1–33) crystal facets of Sn_3O_4 were observable. Compared to pure Sn_3O_4 nanosheets, the XRD peaks of SiNWs/Sn_3O_4 are sharper, indicating that it has better crystallinity. Raman spectrum of SiNWs, Sn_3O_4 and SiNWs/Sn_3O_4 hierarchical heterostructure are shown in Fig. 2b, it can be clearly observed that the Raman spectral peaks of Si at 302, 520, and 937 cm^{-1} and the peaks of Sn_3O_4 at 136, 164 and 234 cm^{-1} [38]. For SiNWs/Sn_3O_4 hierarchical heterostructure, its peak position is well matched to Si and Sn_3O_4, indicating successful synthesis of SiNWs/Sn_3O_4 nanocomposites.

The light absorption properties of the Sn_3O_4 nanosheets and SiNWs/Sn_3O_4 hierarchical heterostructure are measured by a UV–vis diffuse reflectance spectrum (DRS). As shown in the Fig. 2c, the light absorption edge of pure Sn_3O_4 nanosheets is around 500 nm, indicating that it can absorb visible light. After Sn_3O_4 is assembled on SiNWs to form SiNWs/Sn_3O_4 heterostructure, the light absorption range is significantly red-shifted to cover the entire wavelength in the measurement region. This indicates that the heterostructure can better utilize the solar energy, which increases the catalytic efficiency.

The chemical states of SiNWs/Sn_3O_4 hierarchical heterostructure were characterized by X-ray photoelectron spectroscopy (XPS). The survey scan spectra of SiNWs/Sn_3O_4 is shown in Fig. S4. It indicates that the presence of Si, Sn and O elements in the nanocomposite, and the corresponding ratios of Si 2p, O 1s, Sn $3d_{3/2}$, and Sn $3d_{5/2}$ are about 5.5%, 34.4%, 24.3%, and 35.9%, respectively, confirming the successful preparation of Sn_3O_4 on SiNWs. As shown in Fig. 2d, the high-resolution XPS spectra of Sn 3d shows two characteristic peaks of Sn $3d_{5/2}$ and Sn $3d_{3/2}$. For the Sn $3d_{5/2}$, two characteristic peaks can be obtained by curve fitting. They are located at 487.0 and 485.7 eV, respectively. Similarly, the Sn $3d_{3/2}$ spectrum was curve-fitted with two peaks with the binding energies of 495.9 and 494.7 eV [33]. Fig. 2e shows the XPS characteristics of Si 2p in SiNWs/Sn_3O_4 heterostructure. By fitting, two binding energies of Si 2p at 102.6 eV and 103.4 eV can be obtained [39]. From Fig. 2f, it can be observed that the characteristic peaks of O 1s is located at 531.3 eV and 532.7 eV, respectively [40]. All the results above indicate the successful synthesis of the 3D hierarchical heterostructure photoelectrocatalyst.

The photoelectrocatalytic performance of the as-synthetic samples was evaluated under the synergistic effect of light irradiation and external bias. For better comparison, Si wafer/Sn_3O_4 was also synthesized. The photocurrent-potential (J–V) curves obtained using the LSV test are shown in Fig. 3a, it reveals that all samples exhibit larger current density under irradiation than in dark conditions. However, it should be noted that the SiNWs/Sn_3O_4 photoanode exhibits enhanced photocurrent density and remarkably positively shifted onset potential (V_{onset}, defined as the onset potential of cathodic photocurrent, which is the potential corresponding to the zero photocurrent in the polarization
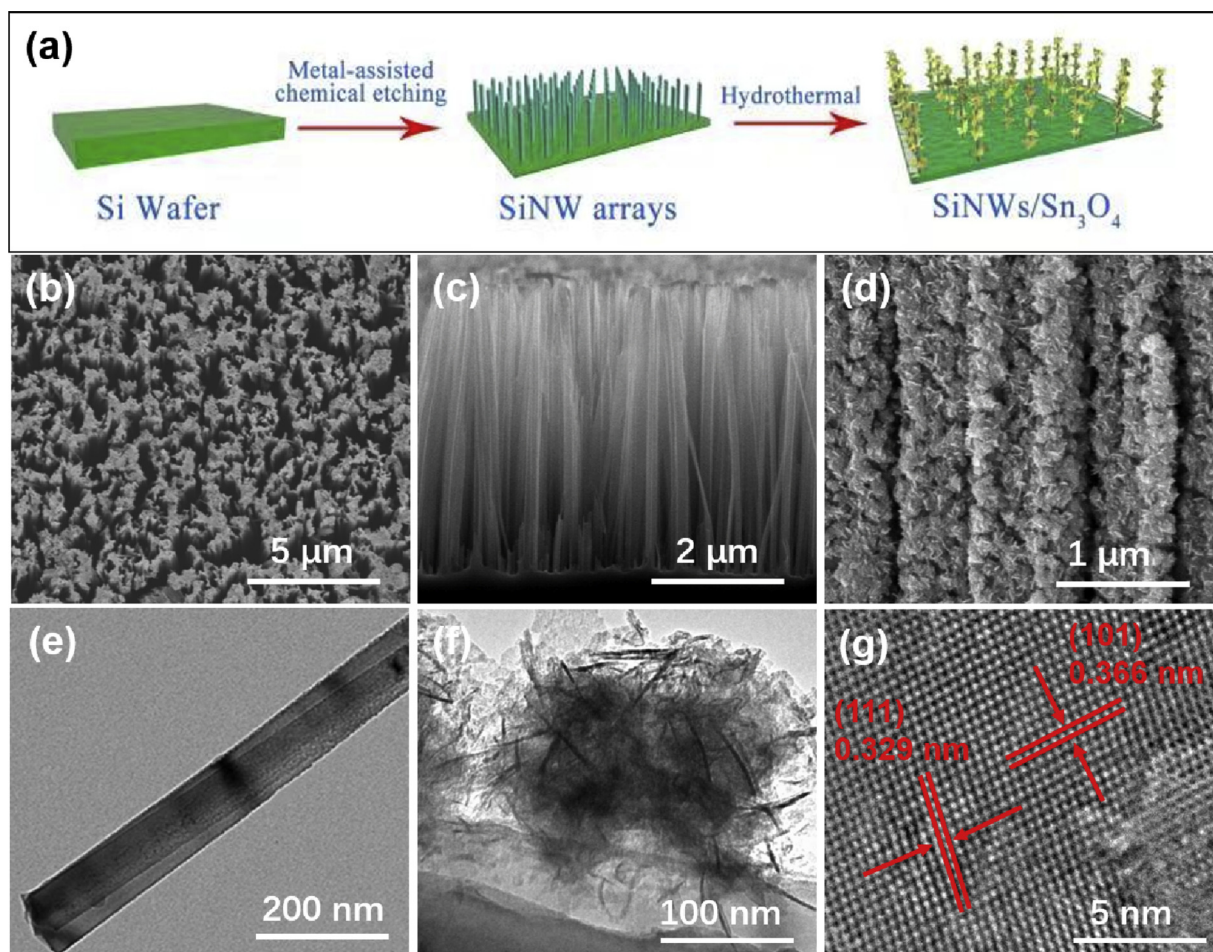
Fig. 1. (a) Schematic diagram of the formation for the SiNWs/Sn_3O_4 nanocomposites. Typical SEM images of (b) plane view and (c) cross-sectional view of SiNWs array and (d) SiNWs/Sn_3O_4 nanocomposites. Typical TEM images of (e) a single Si nanowire and (f) SiNWs/Sn_3O_4 nanocomposite. (g) Typical HRTEM image of Sn_3O_4 nanosheet on the SiNWs.
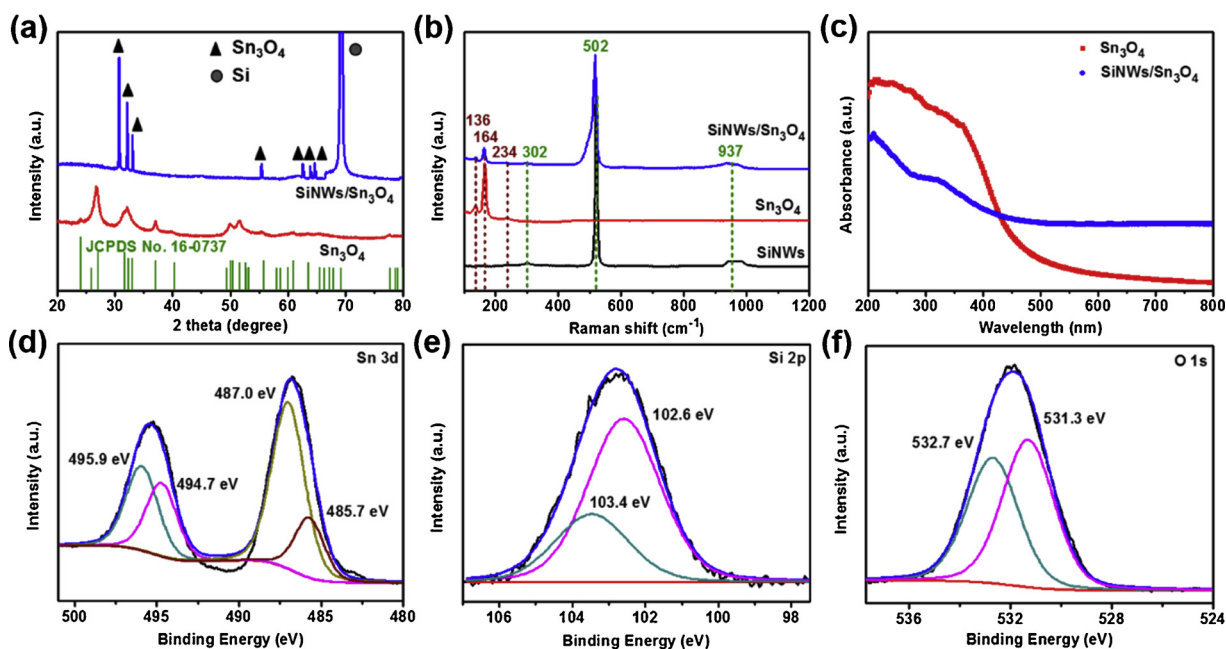
Fig. 2. (a) XRD patterns of Sn_3O_4 and SiNWs/Sn_3O_4 hierarchical heterostructure. (b) Raman spectra of SiNWs, Sn_3O_4 nanosheets and SiNWs/Sn_3O_4 hierarchical heterostructure excited by a 532 nm laser. (c) UV–vis diffuse reflectance spectra of Sn_3O_4 and SiNWs/Sn_3O_4 hierarchical heterostructure. XPS spectra (d) Sn 3d, (e) Si 2p and (f) O 1s peaks for SiNWs/Sn_3O_4 hierarchical heterostructure.
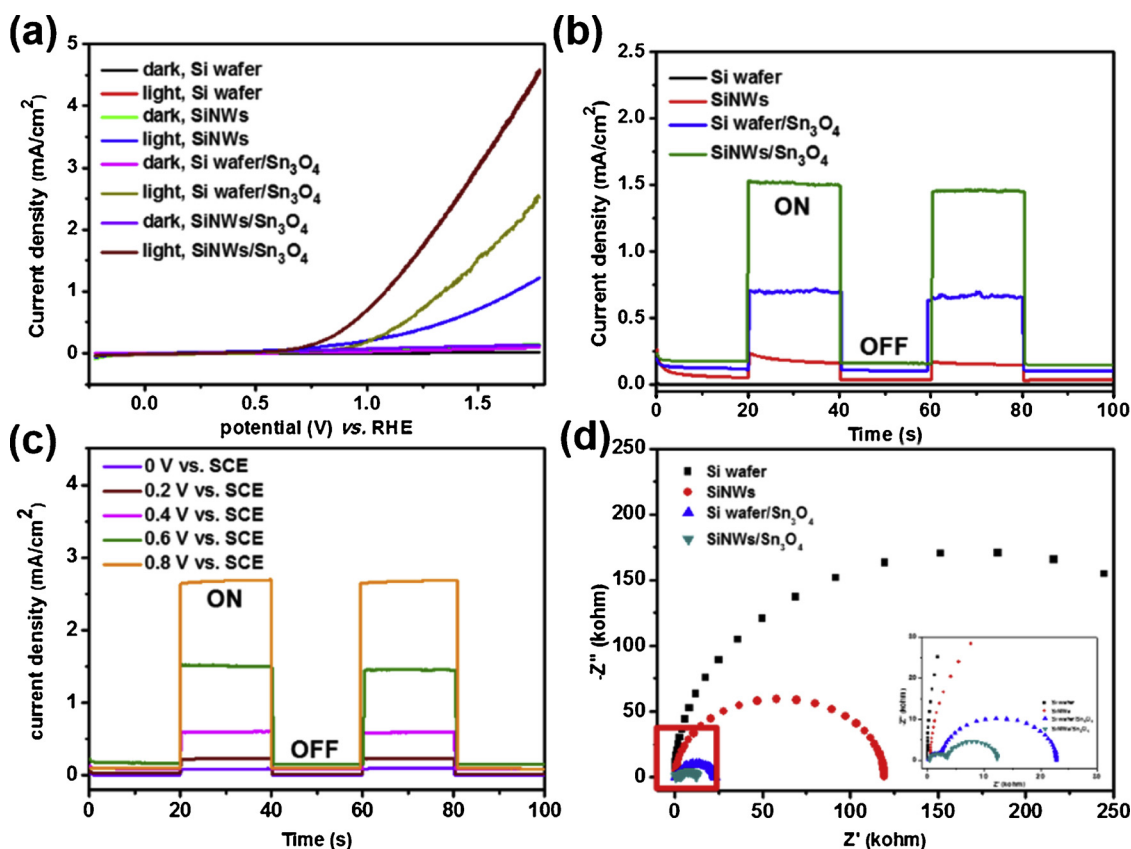
Fig. 3. (a) J–V curves of Si wafer, SiNWs, Si wafer/Sn$_3$O$_4$ and SiNWs/Sn$_3$O$_4$ nanocomposite catalysts in the dark and under irradiation. (b) Instant photocurrent response of synthetic samples at 0.6 V (*vs.* SCE) bias. (c) Instant photocurrent response of SiNWs/Sn$_3$O$_4$ nanocomposite photoanode under different applied voltages. (d) EIS spectra of synthetic samples measured at open circuit voltage, illustration is the enlarged view of the red frame (For interpretation of the references to colour in this figure legend, the reader is referred to the web version of this article).

curve [41]), in comparison with the other samples. It is predicted that the higher current density may result from the unique structure of the SiNWs/Sn$_3$O$_4$ composite that reduces the recombination rate of photoexcited charges.

The instant photocurrent density response of Si wafer, SiNWs, Si wafer/Sn$_3$O$_4$ and SiNWs/Sn$_3$O$_4$ photoanode were measured at 0.6 V (*vs.* SCE) bias to further explain the enhancement of the photoelectrocatalytic properties of SiNWs/Sn$_3$O$_4$ photoanode. Similar behavior to that has been shown in Fig. 3a, when Sn$_3$O$_4$ nanosheets are assembled on SiNWs, the SiNWs/Sn$_3$O$_4$ hierarchical heterostructure photoanode shows excellent photo-switching properties and significantly enhanced photocurrent density. This reveals the reduction of the photogenerated electron/hole pairs recombination rate and effective transport of charge from the inside to the surface of the catalyst, and thus effectively participates in the redox reaction. As can be seen from Fig. 3b, the Si wafer exhibits negligible photocurrent, only 0.001 mA cm^{-2}. The photocurrent densities of the SiNWs and the Si wafer/Sn$_3$O$_4$ are about 0.15 mA cm^{-2} and 0.57 mA cm^{-2}, while the photocurrent of the SiNWs/Sn$_3$O$_4$ heterostructure photoanode approaches 1.3 mA cm^{-2}, which more than 8 times and twice higher than pristine SiNWs and Si wafer/Sn$_3$O$_4$, respectively. This further demonstrates the unique 3D structure and effective coupling of SiNWs/Sn$_3$O$_4$ nanocomposites facilitate enhanced photocatalytic performance. The photocurrent response of SiNWs/Sn$_3$O$_4$ hierarchical heterostructure under different applied voltages is shown in Fig. 3c. The bias voltage is to promote the separation of photoexcited electron-hole pairs by the action of the external electric field, the excess carriers can be used to overcome the large barrier of the catalytic reaction, thereby improving the conversion efficiency of photocatalysis. When the external bias voltage is 0, there is no electric field effect, showing a relatively small photocurrent

response. As the bias voltage increases, the suppression of carrier recombination is enhanced, and the photocurrent response gradually enhanced, thus enhancing the photocatalytic reaction kinetics. This further demonstrates the importance of light and electricity synergy for enhanced catalytic performance.

The incident photo-to-current conversion efficiency (IPCE) was measured to understand the relationship between the photoelectrocatalytic activity and light absorption. The SiNWs/Sn$_3$O$_4$ photoanode exhibits higher photoelectric conversion efficiency than SiNW over the entire wavelength range (Fig. S5), which can be attributed to enhanced photogenerated electron separation efficiency and excellent light harvesting efficiency of unique 3D hierarchical heterojunction structure.

Currently, the electrochemical impedance spectra (EIS) has strong persuasive power in evaluating carrier transfer capability [42], the EIS Nyquist plots of samples can be simulated by the equivalent circuit shown in Fig. S6. The radius of the semicircle in the EIS curves reflects the electron transfer resistance (R$_{ct}$), which can be used to compare the electron transfer kinetics at the photoelectrode/electrolyte interface between different samples. The smaller radius usually shows the lower carrier transfer resistance at interface, which is more conducive to charge transfer [43]. As shown in Fig. 3d and Table S1 (Supporting Information), SiNWs/Sn$_3$O$_4$ heterostructure photoanode has a smaller radius than other samples, it has the smallest R$_{ct}$ value and the largest double-layer capacitance (C$_{dl}$), indicating the fast transfer of carriers at the electrode/electrolyte interface and the efficient separation of electrons and holes. This further proves that the enhancement of the catalytic activity of SiNWs/Sn$_3$O$_4$ photoanode stems from the enhanced charge transport kinetics.

Furthermore, the three-electrode structure was used to detect

(a)

dark light

(b)
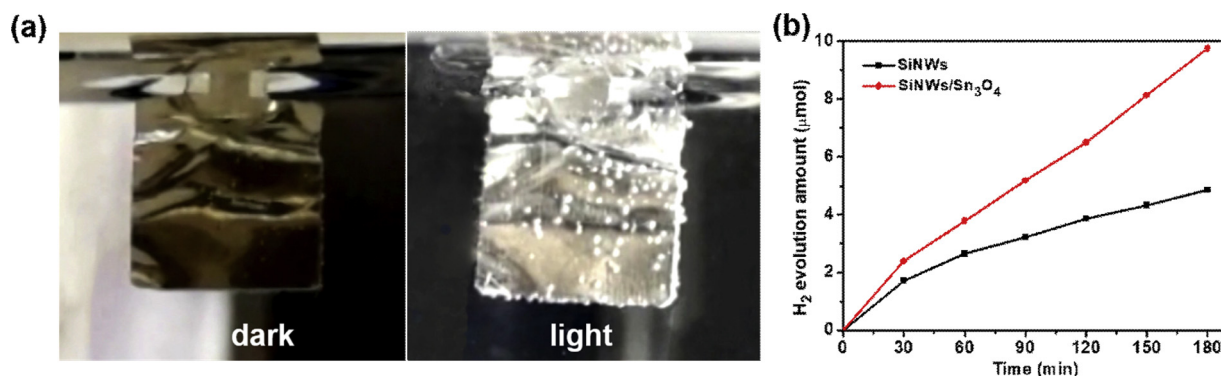
Fig. 4. (a) The photographs of H_2 generation on Pt counter electrode: Off light conditions (left) and on light conditions (right). Using SiNWs/Sn$_3$O$_4$ hierarchical heterostructured array as working electrode for photoelectrocatalytic water splitting. (b) Photoelectrocatalytic H_2 generation of SiNWs and SiNWs/Sn$_3$O$_4$ hierarchical heterostructured array photoanode.

photoelectrocatalytic H_2 production. The photographs (Fig. 4a) and video (Supporting Information) show that only very few bubbles on the platinum electrode are produced in the absence of light. At the moment of turn on the light, the H_2 gas bubbles increased significantly, and with the increase of the illumination time, the bubbles gradually increased. This indicates that the number of carriers increases under light irradiation conditions, and the separation of carriers is facilitated due to the unique structure and high-efficient interface of SiNWs/Sn$_3$O$_4$ photoanode, which is conducive to more carriers to participate in the reaction of water reduction to generate H_2.

To confirm the high H_2 production performance of hierarchical heterostructure photoanode, H_2 production measurement was performed by gas chromatography to assess the catalytic activity of catalysts. The reactions are conducted under continuous voltage and simulated sunlight. The results are shown in Fig. 4b, the amount of generated hydrogen increases linearly with reaction time both for SiNWs and SiNWs/Sn$_3$O$_4$ photoanode. Pure SiNWs shows relatively low water splitting H_2 production activity. Compared with SiNWs, the amount of H_2 generated by SiNWs/Sn$_3$O$_4$ photoanode is increased by about 112%.

To further demonstrate the enhanced performance of synthesized samples, we compared the electrochemical surface area (ECSA) of the SiNWs/Sn$_3$O$_4$ and the SiNWs. SiNWs/Sn$_3$O$_4$ has a larger electrochemical surface area than SiNWs (Fig. S7), indicating more active sites are exposed, which is beneficial to the adsorption and activation of water molecules, thus showing better hydrogen production capacity.

The degradation experiments of organic pigment methylene blue (MB) were used to evaluate the photoelectrocatalytic capability of the synthesized catalysts to further demonstrate the synergistic effect of the SiNWs/Sn$_3$O$_4$ hybrid nanostructures. Since the maximum absorption peak of MB is at 664 nm, 664 nm light was used to evaluate the degradation degree. The concentration of MB at time t (C) and time t = 0 (C$_0$) was measured, and the variety of C/C$_0$ can be used to assess photoelectric degradation ability [44]. The degradation results of different catalysts are shown in the Fig. 5a. The SiNWs and Si wafer/Sn$_3$O$_4$ show a relatively low catalytic degradation activity, and the degradation rate of MB was around 33% and 49% after 180 min, respectively. However, the degradation rate of SiNWs/Sn$_3$O$_4$ can reach 65%. It indicates that the combination of two suitable semiconductors can reduce the recombination rate of photogenerated carriers, thus exhibit higher activity. When SiNWs and Sn$_3$O$_4$ assembled to be a 3D hierarchical heterostructure, its degradation efficiency is higher compared to other catalysts, which may be attributed to the unique 3D structure have a large active surface area, and shortened carrier transport distance, which facilitates the transport of carriers.

The photoelectrocatalytic degradation kinetics of MB over all synthetic samples were also calculated to further understand the degradation process. For all catalysts, it follows the pseudo first-order

kinetics equation for the degradation of MB [45]:

$$\ln(C_t/C_0) = -kt$$

The calculated fitting curve is shown in Fig. 5b. The results show that the kinetic constant (k) of SiNWs for MB degradation process is only $0.00256\,min^{-1}$ and that over Si wafer/Sn$_3$O$_4$ is about $0.00386\,min^{-1}$, the undesired degradation efficiency of SiNWs and Si wafer/Sn$_3$O$_4$ may be attributed to the rapid photo-excited charge recombination rate inside the catalyst. The SiNWs/Sn$_3$O$_4$ photoanode exhibits higher degradation activity than other catalysts, and the kinetic constant is $0.00636\,min^{-1}$ (shown in Fig. 5c). All data indicate that the formation of a unique 3D hierarchical heterostructure promotes charge separation and facilitates charge transport, which is conducive to more charges involved in the redox reactions, thus enhancing the catalytic activity.

In order to further evaluate the impact of light and under bias potential on degradation of MB using SiNWs/Sn$_3$O$_4$ photoanode, we conducted performance measurements under different conditions. As shown in Fig. 5d, after 180 min of testing, there is almost no degradation of MB only applying a potential without light irradiation. The redox potential of MB is 0.523 *vs.* NHE [46], although the applied voltage is greater than the redox potential of MB, the amount of the entire solution is large due to the surface area of the electrode, no significant difference can be seen after 180 min. The degradation rate of MB is just 30% after 180 min with light radiation without applying bias potential. Degradation rate of MB using SiNWs/Sn$_3$O$_4$ hierarchical heterostructure is significantly increased under the coordinated application of light and bias voltage of 0.6 V (*vs.* SCE), and greatly reduce the degradation time. This indicates that the synergistic effect of light and electricity is crucial, and the dominant role is still photocatalysis in photoelectrocatalysis, the bias can further enhance the separation of carriers. As shown in Fig. 5e, the photoelectrocatalytic degradation kinetics of MB over SiNWs/Sn$_3$O$_4$ hierarchical heterostructure under different conditions shows the same result. Fig. 5f shows the absorption spectra of MB degraded with SiNWs/Sn$_3$O$_4$ hierarchical heterostructure at different degradation times. As the irradiation time increases, the absorption of MB in the entire wavelength range significantly decreases, indicating that MB is continuously degraded under light irradiation.

In order to verify the structural stability of the material. The morphology of the SiNWs/Sn$_3$O$_4$ photoanode were investigated by SEM after the photoelectrocatalytic test (Fig. S9). The integrity of the nanowire array structure is well retained, and the Sn$_3$O$_4$ still retains spherical aggregates assembled from nanosheets, exhibiting a morphology similar to that observed in the as-fabricated SiNWs/Sn$_3$O$_4$ photoanode.

Mott-Schottky (M–S) plots were measured to study the band bending at electrode-electrolyte interface [47]. As shown in Fig. 6, both
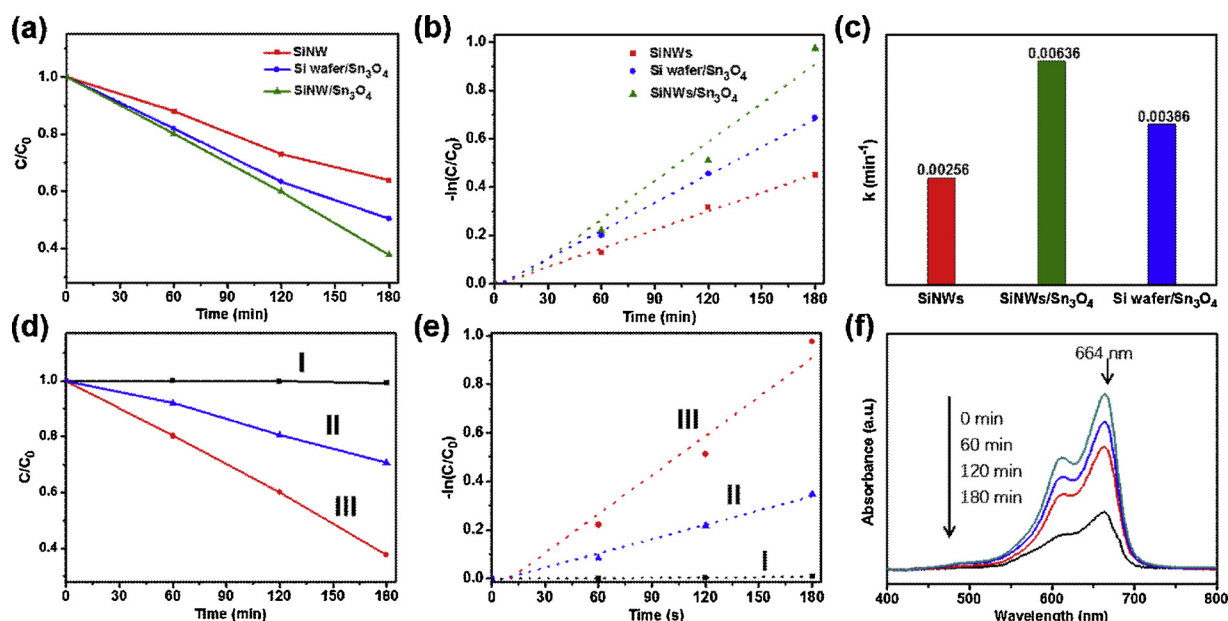
Fig. 5. (a) Degradation degree of MB using SiNWs, Si wafer/Sn_3O_4 and SiNWs/Sn_3O_4 photoanodes under light irradiation at 0.6 V (*vs.* SCE) bias. (b) The kinetics curve and (c) corresponding reaction constant of MB photocatalytic degradations over different samples. (d, e) Degradation degree and kinetics curve of MB using SiNWs/Sn_3O_4 photoanode as catalysts at different conditions: (I) electrocatalytic degradation of MB with an applied bias of 0.6 V (*vs.* SCE); (II) photocatalytic degradation under light irradiation; (III) photoelectrocatalytic degradation with light irradiation at 0.6 V (*vs.* SCE) bias. (f) Absorption spectra of MB with irradiation time over SiNWs/Sn_3O_4 nanocomposite catalysts.

SiNWs and SiNWs/Sn_3O_4 show a positive slope indicating that they are all n-type semiconductors [48]. The flat band potentials (E_{fb}) of the SiNWs and SiNWs/Sn_3O_4 are -0.06 V and -0.49 V (*vs.* SCE). As a result, the potential of conductive bands of SiNWs/Sn_3O_4 is about −0.49 V, which is 0.43 V higher than that of pure SiNWs, indicating that the SiNWs/Sn_3O_4 has stronger oxidation capacity than SiNWs. Moreover, the M–S relation is given below [49]:

$$\frac{1}{C_{sc}^2} = \frac{2}{eA^2\varepsilon_r\varepsilon_0 N_D}\left(E - E_{fb} - \frac{KT}{e}\right)$$

Here C_{sc} and A are the interfacial capacitance and area, respectively, N_D is the charge carrier density, ε_0 is permittivity in vacuum, ε_r is the relative permittivity, E is the applied voltage, K is Boltzmann's constant, T is the absolute temperature, and e is the electronic charge. From Fig. 6, N_D can be calculated by slope (k) using the formula of $N_D = (2/e_0\varepsilon_0\varepsilon_r)/k$. SiNWs/$Sn_3O_4$ hierarchical heterostructured array photoanode shows a smaller slope than SiNWs, thus SiNWs/Sn_3O_4 has a larger carrier density. This likely attributed to the enhanced photoelectrocatalytic water splitting to H_2 production reaction kinetics at the SiNWs/Sn_3O_4 electrode-electrolyte interface and the excellent carrier separation efficiency of the nanocomposite. All the above data prove once again that
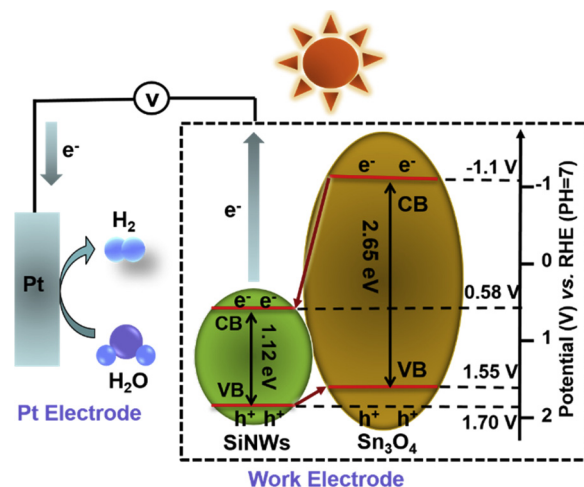
Fig. 7. Schematic diagram of electron transfer in the SiNWs/Sn_3O_4 hierarchical heterostructure photoanode.
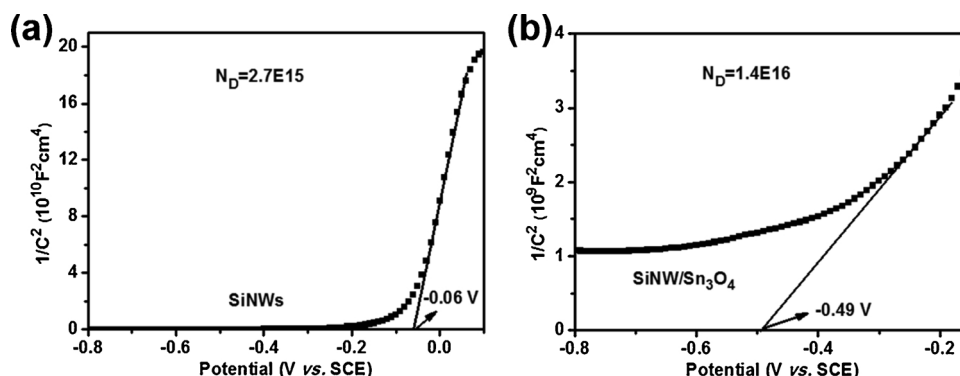
Fig. 6. Mott-Schottky images of (a) pristine SiNWs and (b) SiNWs/Sn_3O_4 hierarchical heterostructured array photoanode.

SiNWs/Sn$_3$O$_4$ hierarchical heterostructured array photoanode has superior catalytic activity (Fig. 7).

Through all the above studies, a possible charge transport mechanism for photoelectrocatalytic enhancement of SiNWs/Sn$_3$O$_4$ hierarchical heterostructure is proposed. As we all know, the conduction band potential of n-type semiconductors lies close to the E$_{fb}$ [50]. Therefore, the conduction band (CB) and valence band (VB) positions of SiNWs are at 0.58 V and 1.70 V vs. RHE, respectively. In this system, a typical type-II heterojunction is formed. Under light irradiation, the semiconductors are excited to generate electrons and holes. Due to the appropriate bandgap positions of the two semiconductors and the potentials of VB and CB of Sn$_3$O$_4$ are higher than those of SiNWs, the photo-excited electrons are transmitted from the CB of Sn$_3$O$_4$ to the CB of SiNWs, while the holes remaining on the VB are shifted in the opposite direction. Effective separation of photogenerated electron-hole pairs through this migration route. Then, the electrons on CB of SiNWs are transferred to the counter electrode through the external circuit due to the applied voltage, and undergoes the redox reaction with the H$^+$ to generate H$_2$. In summary, the photoelectrocatalytic reaction of ultrafine SiNWs/Sn$_3$O$_4$ photoanode followed a type-II mechanism, which not only inhibits the recombination of photo-excited electron-hole pairs, but also accelerates charge transfer to maintain excellent redox reactions.

3. Conclusion

In conclusion, a 3D SiNWs/Sn$_3$O$_4$ hierarchical heterostructured array photoanode have been successfully synthesized by the metal-assisted chemical etching following hydrothermal method. By etching the ultrafine nanowires array structure, the absorption capacity can be further enhanced. Sn$_3$O$_4$ in-situ grown on the Si nanowires ensures more active sites and faster photocarrier transfer. More importantly, the heterostructure formed between Sn$_3$O$_4$ and Si promote the directional transport of carriers. With the enhanced light harvesting, efficient photogenerated electron-hole separation and rapid charge transfer at the photoanode, and excellent photoelectrocatalytis activity has been realized, inculidng the photoelectrochemical degradation and H$_2$ production. The methods and results presented in this work provide a new strategy for building high-efficiency 3D Si-based hierarchical heterojunction photoanode for photoelectrocatalytic solar energy conversion.

4. Experimental section

4.1. Materials

The Si wafers (n type, 100 oriented, 3–8 Ω cm) were obtained through Tianjin Institute of Semiconductor Technology. Tin(II) chloride dihydrate (SnCl$_2$·2H$_2$O), trisodium citrate dehydrate (Na$_3$C$_6$H$_5$O$_7$·2H$_2$O), sodium sulfate (Na$_2$SO$_4$), silver nitrate (AgNO$_3$), sodium hydroxide (NaOH), hydrofluoric acid (HF), hydrogen peroxide (H$_2$O$_2$), acetone and ethanol were purchased from Sinopharm Chemical Reagent Corporation Ltd which are of reagent grade and used without further purification. Deionized water was further purified with a Miniport water purification device (Millipore, Bedford, MA, USA).

4.2. Synthesis of SiNWs

SiNWs were synthesized by common metal-assisted chemical etching (MACE) [26]. Specifically, the Si wafer (n type, 100 oriented, 3–8 Ω·cm) was ultrasonicated in sequence in acetone, ethanol and deionized water each for 10 min to remove grease, subsequently transferred to 5% HF for 10 min to decompose oxide layer formed at surface. The initially treated Si wafer was quickly transferred to a solution containing 4.8 M HF and 5 mM AgNO$_3$, and the solution was slowly stirred for 1 min to form a layer of silver nanoparticles on the surface of the Si wafer. Then rinsed the wafer repeatedly with deionized

water to remove excess Ag$^+$ ions. Next, the Si wafer with a layer of silver nanoparticles on the surface was transferred to the etchant solution composed of 4.6 M HF and 0.5 M H$_2$O$_2$ and let it stand at room temperature for 40 min. The etched Si wafer was washed with deionized water and rapidly transferred to nitric acid solution for 15 min to remove silver nanoparticles. In order to remove the oxide layer formed on the surface, the wafer was transferred again to 5% HF for 15 min. Finally, the wafer was cleaned with deionized water and blown dry with nitrogen.

4.3. Synthesis of SiNWs/Sn$_3$O$_4$

The Sn$_3$O$_4$ nanosheets grew in situ on the SiNWs array by a hydrothermal method. Specifically, 5.0 mmol SnCl$_2$·2H$_2$O and 12.5 mmol Na$_3$C$_6$H$_5$O$_7$·2H$_2$O were dissolved in 25 mL of deionized water, and subjected to ultrasonication and stirring for 10 min, respectively. Then 12.5 mL of 0.2 M NaOH was added to the solution under constant stirring, followed by ultrasonic treatment. The above solution was transferred to a 50 mL Teflon-lined stainless-steel autoclave and added the previously prepared SiNWs of certain specifications in it, heated at 180 °C for 12 h. The samples collected after treatment were rinsed several times with deionized water and dried at 60 °C for 8 h.

4.4. Characterizations

The morphology and the structure of all the samples were characterized using HITACHIS-4800 field-emission scanning electron microscope (FE-SEM) and high-resolution transmission electron microscope (HR-TEM, JEM2100 F). X-ray powder diffraction (XRD) patterns of samples were detected by the Bruker D8 Advance powder X-ray diffractometer with Cu-Kα radiation (λ = 0.15406 nm). The UV–vis diffuse reflectance spectra were measured at room temperature in the range of 200–800 nm on a UV–vis spectrophotometer (UV-3101PC, Shimadzu) and with BaSO$_4$ as the reflectance standard. The surface chemical species of the samples were determined with a PHI 5000 Versa Probe X-ray photoelectron spectrometer (XPS). Raman spectra measurements were carried out using a confocal microscopic Raman spectrometer with the 532 nm laser light irradiation from 100 to 1200 cm^{-1}.

4.5. Photoelectrochemical measurement

In this section, an electrochemical workstation (CHI 660E, CH Instrument) was used for photoelectrochemical testing. The synthesized catalysts were used as working electrode (the working electrode used in this section has the same size of 1 cm × 1 cm), the reference electrode was saturated calomel electrode (SCE), and the Pt sheet as counter electrode to constitute a standard three-electrode cell structure. The electrolyte was Na$_2$SO$_4$ solution (0.5 M, pH = 6.8), and in order to remove oxygen from the solution, it was bubbled with nitrogen for 20 min before testing. Conversion between standard hydrogen electrode (RHE) potential and saturated calomel electrode potential by the following equation [45]:

$$E(RHE) = E(SCE) + 0.0591 \times pH + 0.245 \text{ V}$$

In a typical PEC test, the light source used was the 300 W xenon lamp equipped with AM 1.5 G filter, and the light density was adjusted to 100 mW/cm^2 prior to each testing. The photocurrent and dark current curves of the synthesized different electrodes were measured by linear scan voltammetry (LSV). The bias range was from −1 V to 1 V (vs. SCE), and the scan rate was 10 mV/s. The instantaneous photocurrent response (I–t) of the different electrodes were tested under the condition of alternating on-off light at a bias of 0.6 V (vs. SCE). The electrochemical impedance spectra (EIS) of the different electrodes were obtained over a range from 10 kHz to 10 mHz at open circuit

voltage. The Mott-Schottky (M–S) plots of the electrodes were obtained at a fixed frequency of 1000 Hz. The cyclic voltammetry (CV) experiments were performed at different scan rate of 40–120 mV/s. Incident photon-to-current quantum conversion efficiency (IPCE) was measured using a monochromator (Newport 74004-1) and an electrochemical workstation (CHI 660E, CH Instrument). The IPCE of the SiNWs and SiNWs/Sn$_3$O$_4$ were analyzed according to the equation:

IPCE = 1240 J/λ P$_{light}$

Where λ is the incident wavelength, J and P$_{light}$ are the measured photocurrent and light intensity at wavelength λ, respectively.

4.6. Photoelectrocatalytic dye degradation

To study the photoelectrocatalytic activity of the photoanode catalysts, we carried out the photoelectrocatalytic degradation of methylene blue (MB). In a typical experiment, the standard three-electrode cell structure was used. The working electrode was the synthetic catalyst of a certain size (1 cm × 1 cm), the SCE acted as the reference electrode, and Pt was the counter electrode. All electrodes were inserted into a 60 mL mixed solution consisting of 0.5 M Na$_2$SO$_4$ and 10 ppm MB, and putted a magnetic stirrer underneath for slow stirring. During the catalytic reaction, a 300 W xenon lamp equipped with AM 1.5 G filter (100 mW/cm^2) was used for illumination and the bias voltage of 0.6 V (*vs.* SCE) was applied. A constant volume of aliquots was sampled at certain irradiation time intervals, then the clear liquor was analyzed using an UV–vis spectrophotometer and recorded the absorbance at the maximum absorption wavelength to monitor the dye concentrations.

4.7. Photoelectrocatalytic water splitting

The photoelectrocatalytic H$_2$ evolution experiments were carried out under the synergistic effect of light and applied voltage. Simply, similar to the above test conditions, the catalytic reaction adopted three-electrode configurations, the certain size of sample (1 cm × 1 cm) as working electrode, the reference electrode was SCE, and the counter electrode was Pt sheet. The efficiency of hydrogen production was measured under the synergy of applied voltage of 1.5 V (*vs.* SCE) and simulated solar radiation with the photocurrent density of 100 mW/cm^2. The hydrogen generation from water splitting was analyzed use an online gas chromatograph (GC-7920) equipped with a thermal conductivity detector.

Notes

The authors declare no competing financial interest.

Appendix A. Supplementary data

Supplementary material related to this article can be found, in the online version, at doi:https://doi.org/10.1016/j.apcatb.2019.117798.

References

[1] A. Landman, H. Dotan, G.E. Shter, M. Wullenkord, A. Housijia, A. Maljusch, G.S. Grader, A. Rothschild, Nat. Mater. 16 (2017) 646-615.
[2] I. Roger, M.A. Shipman, M.D. Symes, Nat. Rew. Chem. 1 (2017) 0003.
[3] D. Dai, H. Xu, L. Ge, C. Han, Y. Gao, S. Li, Y. Lu, Appl. Catal. B-Environ. 217 (2017) 429–436.
[4] L. Yang, Y. Xiong, W. Guo, M. Zhou, K. Zhou, K. Song, P. Xiao, G. Cao, Nano Energy 44 (2018) 63–72.
[5] H. Zhang, Q. Ding, D. He, H. Liu, W. Liu, Z. Li, B. Yang, X. Zhang, L. Lei, S. Jin, Energy Environ. Sci. 9 (2016) 3113–3119.
[6] J. Liu, Y. Liu, N. Liu, Y. Han, X. Zhang, H. Huang, Y. Lifshitz, S.-T. Lee, J. Zhong, Z. Kang, Science 347 (2015) 970–974.
[7] Y. Zhang, J. Liu, Y. Zhang, Y. Bi, Nano Energy 51 (2018) 504–512.
[8] A. Fujishima, K. Honda, Nature 238 (1972) 37–38.
[9] X. Yu, Z. Zhao, D. Sun, N. Ren, L. Ding, R. Yang, Y. Ji, L. Li, H. Liu, Chem. Comm. 54 (2018) 6056–6059.
[10] H. Zhao, G. Liu, F. Vidal, Y. Wang, A. Vomiero, Nano Energy 53 (2018) 116–124.
[11] Y. Liu, S. Ding, Y. Shi, X. Liu, Z. Wu, Q. Jiang, T. Zhou, N. Liu, J. Hu, Appl. Catal. B-Environ. 234 (2018) 109–116.
[12] X. Yu, S. Wang, X. Zhang, A. Qi, X. Qiao, Z. Liu, M. Wu, L. Li, Z.L. Wang, Nano Energy 46 (2018) 29–38.
[13] P. Lianos, Appl. Catal. B-Environ. 210 (2017) 235–254.
[14] X.Q. Bao, M. Fatima Cerqueira, P. Alpuim, L. Liu, Chem. Commun. 51 (2015) 10742–10745.
[15] Y. Dai, X. Wang, W. Peng, C. Xu, C. Wu, K. Dong, R. Liu, Z.L. Wang, Adv. Mater. 30 (2018).
[16] A. Kargar, K. Sun, Y. Jing, C. Choi, H. Jeong, Y. Zhou, K. Madsen, P. Naughton, S. Jin, G.Y. Jung, D. Wang, Nano Lett. 13 (2013) 3017–3022.
[17] J. Zheng, Y. Lyu, C. Xie, R. Wang, L. Tao, H. Wu, H. Zhou, S. Jiang, S. Wang, Adv. Mater. (2018) e1801773.
[18] K. Sun, N. Park, Z. Sun, J. Zhou, J. Wang, X. Pang, S. Shen, S.Y. Noh, Y. Jing, S. Jin, P.K.L. Yu, D. Wang, Energy Environ. Sci. 5 (2012) 7872–7877.
[19] S.M. Thalluri, J. Borme, K. Yu, J. Xu, I. Amorim, J. Gaspar, L. Qiao, P. Ferreira, P. Alpuim, L. Liu, Nano Res. 11 (2018) 4823–4835.
[20] S.W. Boettcher, E.L. Warren, M.C. Putnam, E.A. Santori, D. Turner-Evans, M.D. Kelzenberg, M.G. Walter, J.R. McKone, B.S. Brunschwig, H.A. Atwater, N.S. Lewis, J. Am. Chem. Soc. 133 (2011) 1216–1219.
[21] L. Zhang, C. Liu, A.B. Wong, J. Resasco, P. Yang, Nano Res. 8 (2015) 281–287.
[22] J. Moon, U. Sim, D.J. Kim, H.-Y. Ahn, J. An, H. Ha, K.S. Choi, C. Jeon, J. Lee, K.T. Nam, B.H. Hong, Nanoscale 10 (2018) 13936–13941.
[23] Z. Chen, G. Ma, Z. Chen, Y. Zhang, Z. Zhang, J. Gao, Q. Meng, M. Yuan, X. Wang, J.-M. Liu, G. Zhou, Appl. Surf. Sci. 396 (2017) 609–615.
[24] J.B. Hannon, S. Kodambaka, F.M. Ross, R.M. Tromp, Nature 440 (2006) 69–71.
[25] B. Fuhrmann, H.S. Leipner, H.-R. Hoche, L. Schubert, P. Werner, U. Gosele, Nano Lett. 5 (2005) 2524–2527.
[26] Z. Huang, N. Geyer, P. Werner, J. de Boor, U. Goesele, Adv. Mater. 23 (2011) 285–308.
[27] H.-X. Han, C. Shi, N. Zhang, L. Yuan, G.-P. Sheng, Sci. Total Environ. 639 (2018) 1512–1519.
[28] I. Oh, J. Kye, S. Hwang, Nano Lett. 12 (2012) 298–302.
[29] T. Hisatomi, J. Kubota, K. Domen, Chem. Soc. Rev. 43 (2014) 7520–7535.
[30] X. Li, X. Meng, J. Liu, D. Geng, Y. Zhang, M.N. Banis, Y. Li, J. Yang, R. Li, X. Sun, M. Cai, M.W. Verbrugge, Adv. Funct. Mater. 22 (2012) 1647–1654.
[31] J. Wang, N. Umezawa, H. Hosono, Adv. Energy Mater. 6 (2016).
[32] X. Yu, Z. Zhao, D. Sun, N. Ren, J. Yu, R. Yang, H. Liu, Appl. Catal. B-Environ. 227 (2018) 470–476.
[33] L. Zhu, H. Lu, D. Hao, L. Wang, Z. Wu, L. Wang, P. Li, J. Ye, ACS Appl. Mater. Interfaces 9 (2017) 38537–38544.
[34] H. Song, S.-Y. Son, S.K. Kim, G.Y. Jung, Nano Res. 8 (2015) 3553–3561.
[35] M. Manikandan, T. Tanabe, P. Li, S. Ueda, G.V. Ramesh, R. Kodiyath, J. Wang, T. Hara, A. Dakshanamoorthy, S. Ishihara, K. Ariga, J. Ye, N. Umezawa, H. Abe, ACS Appl. Mater. Interfaces 6 (2014) 3790–3793.
[36] X. Yu, Z. Zhao, N. Ren, J. Liu, D. Sun, L. Ding, H. Liu, ACS Sustain. Chem. Eng. 6 (2018) 1175–1782.
[37] Y. Yang, M. Wang, P. Zhang, W. Wang, H. Han, L. Sun, ACS Appl. Mater. Interfaces 8 (2016) 30143–30151.
[38] X. Chen, Y. Huang, K. Zhang, X. Feng, M. Wang, Electrochim. Acta 259 (2018) 131–142.
[39] D. Wu, Z. Lou, Y. Wang, Y. Wang, Z. Yao, T. Xu, Z. Shi, J. Xu, Y. Tian, X. Li, Y.H. Tsang, Sol. Energy Mater. Sol. Cells 182 (2018) 272–280.
[40] X. Yu, L. Wang, J. Zhang, W. Guo, Z. Zhao, Y. Qin, X. Mou, A. Li, H. Liu, J. Mater. Chem. A 3 (2015) 19129–19136.
[41] C. Lv, Z. Chen, Z. Chen, B. Zhang, Y. Qin, Z. Huang, C. Zhang, J. Mater. Chem. A 3 (2015) 17669–17675.
[42] T. Wu, Y. Zhang, D. Wei, X. Wang, T. Yan, B. Du, Q. Wei, Sensor Actuat. B-Chem. 256 (2018) 812–819.
[43] M. Basu, Z.-W. Zhang, C.-J. Chen, P.-T. Chen, K.-C. Yang, C.-G. Ma, C.C. Lin, S.-F. Hu, R.-S. Liu, Angew. Chem. Int. Ed. 54 (2015) 6211–6216.
[44] W.-K. Jo, N.C.S. Selvam, Chem. Eng. J. 317 (2017) 913–924.
[45] X. Yu, Z. Zhao, J. Zhang, W. Guo, L. Li, H. Liu, Z.L. Wang, CrystEngComm 19 (2017) 129–136.
[46] W. Zhang, M. Caldarola, B. Pradhan, M. Orrit, Angew. Chemie Int. Ed 56 (2017) 3566–3569.
[47] Z. Xu, Z. Guan, J. Yang, Q. Li, ACS Appl. Energy Mater. 2 (2019) 2779–2785.
[48] J. Wang, W. Jiang, D. Liu, Z. Wei, Y. Zhu, Appl. Catal. B-Environ. 176-177 (2015) 306–314.
[49] C. Tian, M. Jiang, D. Tang, L. Qiao, H. Xiao, F.E. Oropeza, J. Mater. Chem. A 7 (2019) 11895–11907.
[50] D.E. Schipper, Z. Zhao, A.P. Leitner, L. Xie, F. Qin, M.K. Alam, S. Chen, D. Wang, Z. Ren, Z. Wang, J. Bao, K.H. Whitmire, ACS Nano 11 (2017) 4051–4059.